

Precoder Implementation and Optimization in 5G NR Massive MIMO Radio

Kalyani Bhukya^{*}, Shahid Aamir Sheikh[†], Radha Krishna Ganti[‡]

Department of Electrical Engineering

Indian Institute of Technology Madras

Email: ^{*}ee21s124@smail.iitm.ac.in, [†]shahidaamir100@tamu.edu, [‡]rganti@ee.iitm.ac.in

Abstract—The evolution of 5G New Radio (NR) has brought significant improvements in signal strength and service quality for users. By the integration of Multiple Input Multiple Output (MIMO) systems in communications, multiple data streams can be transmitted simultaneously across multiple antennas. Additionally, the incorporation of precoding in MIMO systems enables enhanced data rates and spectral efficiency. In the case of wireless networks, precoders are used to steer high-gain beams that are intended for specific users. The paper focuses on the implementation of 16, 32 and 64 channel linear precoders in the Remote Radio Head (RRH) of the indigenously developed 5G testbed at IIT Madras. These precoders have a memory module which stores the channel matrices and a multiplier module which performs matrix multiplications between the channel matrices and user data within a slot duration of 500 microseconds. The system demonstrates DSP utilization levels of 9.75%, 19.5%, and 39% for (16×8) , (32×8) , and (64×8) antenna-layer configurations respectively, while maintaining the BRAM (Block RAM) usage within 2.28%, 3.91%, and 7.16%. Additionally, a throughput of 1.2 Gbps with four active layers highlights the system's optimized performance under hardware constraints.

Index Terms—5G NR, MIMO, Beams, Remote Radio Head, O-RAN, FPGA, DSP.

I. INTRODUCTION

The emergence of 5G New Radio (NR) technology aims to address the increasing demand for higher data rates, enhanced reliability, and ultra-low latency communication [1]. A key enabler of these capabilities is the adoption of massive MIMO (Multiple Input Multiple Output) systems, which employ a large number of antennas at the base station (BS) to serve multiple users simultaneously. To fully leverage massive MIMO, the implementation of precoders is essential, as they shape transmitted signals to improve signal quality and reduce interference for the users. This makes precoding a crucial factor in achieving high throughput and effective beamforming.

Efficient precoding requires complex matrix multiplications under strict timing constraints, which typically lies within a $500\mu\text{s}$ slot duration [2]. Due to the heavy computational demand of traditional complex multipliers, Karatsuba's technique is utilized to reduce the load [3]. FPGA-based implementations, particularly for massive MIMO systems, aim to optimize speed, resource usage, and power efficiency [4]. Several studies highlight the importance of pipelining, fixed-point arithmetic, and hardware-optimized algorithms to meet performance requirements [5]. Despite the advances, balancing low-latency processing with resource efficiency remains

challenging for real-time applications. This paper focuses on optimizing FPGA-based linear precoding for massive MIMO systems.

The current precoder implementation and optimization for massive MIMO configurations, with antenna-layer pairs represented as $(N_T, N_L) = (16 \times 8)$, (32×8) , and (64×8) , where N_T indicates the number of transmit antennas and N_L is the number of layers. By evaluating matrix storage and multiplication techniques, and by efficient utilization of DSP resources, it has been demonstrated that real-time processing can be achieved at frequencies of 250 MHz for multipliers and 312.5 MHz for memory access.

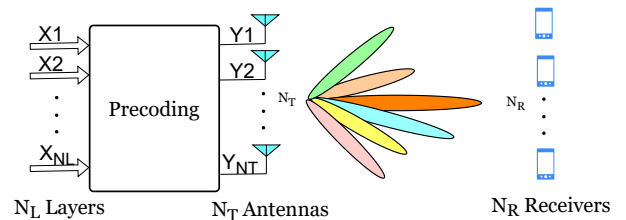


Fig. 1: Precoding/Beamforming

Fig. 1 illustrates the precoding and beamforming process, where multiple antennas direct the signals to various users. The implementation discussed in this paper supports adaptive beamforming, enabling both narrow and wide beams to suit diverse user requirements in 5G networks.

The current paper is organized as follows: Section II provides the architecture required to build the downlink precoder. Section III describes the data flow taking place in the precoder. Section IV gives a detailed explanation of the testing and evaluation methods adopted in the current work. Section V reports the performance of the precoder design and discusses its effect on hardware utilization. Section VI provides the future directions that can be taken in precoder development in 5G NR.

II. ARCHITECTURE OVERVIEW

In a 5G system [6], the downlink data flows from the Baseband Unit (BBU) to the Radio Remote Head (RRH) through the ORAN architecture [7]. The BBU processes the control and user plane data before passing it to the precoder, which receives configuration and data information.

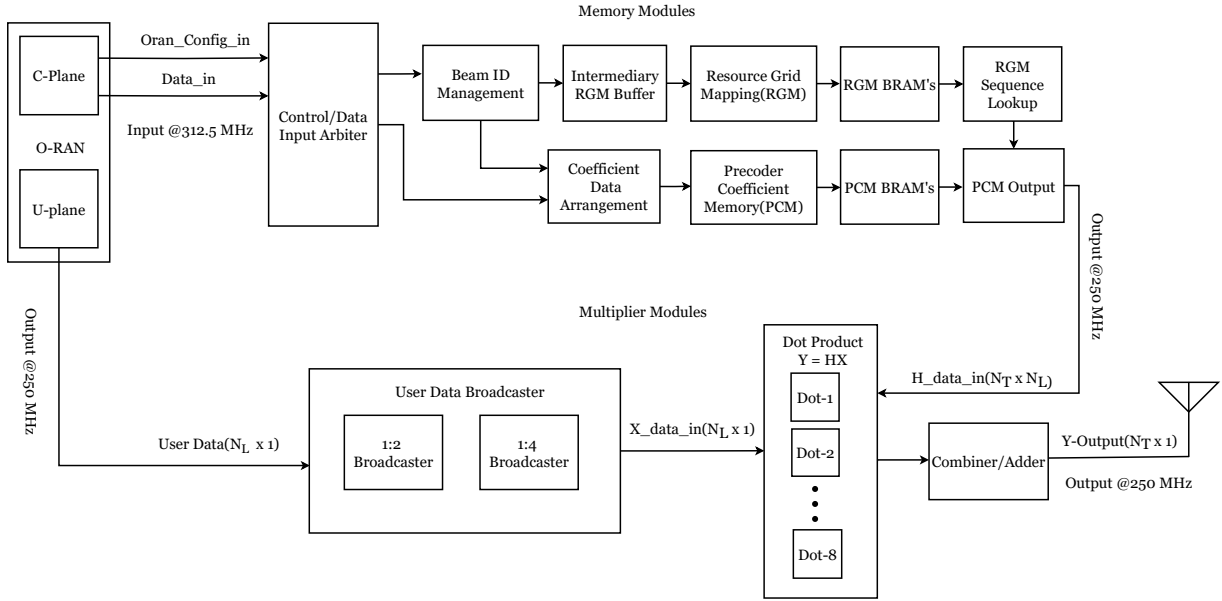


Fig. 2: Downlink Precoder Architecture: data processing and transmission flow from O-RAN to precoder

The precoder then generates the beamforming data, which is then forwarded to the digital front-end module for further processing, such as IFFT and guard band addition [2]. The precoder consists of two major entities, namely, the memory module and matrix multiplier module operate sequentially to achieve this functionality. The detailed explanation of these modules is in the subsequent subsections.

A. Open-Radio Access Network (O-RAN)

The O-RAN module serves as the primary interface for providing inputs to the precoder, through the two major planes: the control plane (C-plane) and the user plane (U-plane).

- 1) Control plane (C-plane): The C-plane conveys control information to the precoder. This includes resource allocation, scheduling parameters, and beam configurations. It helps to map beamforming coefficients to the corresponding antenna ports using beam ID.
- 2) User plane (U-plane): The U-plane carries user data as IQ samples, which are mapped to resource elements based on the number of layers. This mapping enables the precoder to allocate data to the appropriate layers and antenna ports for efficient transmission.

B. Memory module

The precoder memory module in the RRH is responsible for scheduling and storing precoding matrices for upcoming transmission slots. Leveraging a two-slot look-ahead structure, as highlighted in [2], it ensures the availability of real-time data. The module supports up to 64 user precoder matrices per slot and incorporates a ping-pong architecture, enabling simultaneous read and write operations. The clock domain crossings are efficiently managed using the XPM-CDC macros, ensuring reliable data transfer between the input and

output domains. The various components within the memory subsystem (See Fig.2) and their functions are as follows:

- 1) Control/Data input arbiter: This stage is responsible for accurately loading control and data packets into their respective pipelines in the correct order. The control packet includes input parameters such as slot_ID, start_symbol, num_symbol, start_PRB, num_PRB, beam_ID, Bundle_PRB and Re_Mask.
- 2) Beam ID roster management: This stage is responsible for maintaining a ledger of all beam IDs encountered within the current slot and assigning each one with a unique Internal Address Number (IAN). The beam ID is a 16-bit unique identifier that contains beamforming information as specified in the 3rd Generation Partnership Project (3GPP) standards [8].
- 3) Intermediate resource grid mapping (RGM) buffer: RGM is a variable cycle operation, hence a buffer is inserted here so that the output of beam ID roster management can be stored and processed in sequence.
- 4) Resource Grid Mapping (RGM) input: The RGM module retrieves scheduling information from the RGM buffer. It fills the resource grid with IANs (beam IDs) and sets a valid bit for successful writes. For unallocated PRBs, the valid bit remains unset, signaling the output to send zeros to conserve bandwidth. A ping-pong buffering scheme clears the RG before each write to support a two-slot look-ahead structure. Each RGM is $273 \times 14 \times (7+1) = 30,576$ bits, allowing up to 4 IANs per cycle with a 32-bit input. To handle a 1024-cycle write overhead, two memory banks with 4 BRAMs each can be used as shown in the Fig.???. Upon reset, Bank 0 (BRAM 0 and BRAM 1) and Bank 1 (BRAM 2) are wiped sequentially. After this initialization, subsequent

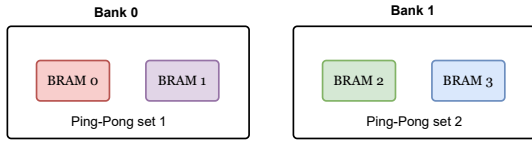


Fig. 3: RGM Ping Pong buffering

TABLE I: RGM-BRAM operations with color coding

		2'b00	2'b01	2'b10	2'b11
		RGM BRAM 0	RGM BRAM 1	RGM BRAM 2	RGM BRAM 3
	RESET	Wipe	Wipe	Wipe	
SLOT 0	REG OPR	Write			
SLOT 1	REG OPR	Read	Write		Wipe
SLOT 2	REG OPR	Wipe	Read	Write	
SLOT 3	REG OPR		Wipe	Read	Write

operations (wiping, reading, and writing) are performed in parallel across the banks, as illustrated in the Table I.

- 5) Input coefficient data arrangement: The precoding multiplier requires matrix to be formatted in a specific order, which differs from the way O-RAN delivers data to the memory module. Before writing to the Precoding Coefficient Memory (PCM), the input data is rearranged so that all even coefficients of the first column are read first, followed by the odd coefficients of the same column.
- 6) Precoder Coefficient Memory (PCM) input: This stage is responsible for selecting the appropriate ping-pong memory buffer for storing the PCM data.
- 7) RGM Sequence Lookup: Upon a read trigger, this stage retrieves the sequence of precoder matrices and initiates their reading from the PCM for transmission. Additionally, it communicates the number of times each matrix should be reused and indicates whether to load a new matrix through the mult_cfg port.

TABLE II: TX precoder coefficient matrix output format

r0c0	r0c1	r0c2	r0c3	r0c4	r0c5	r0c6	r0c7
r1c0	r1c1	r1c2	r1c3	r1c4	r1c5	r1c6	r1c7
r2c0	r2c1	r2c2	r2c3	r2c4	r2c5	r2c6	r2c7
r3c0	r3c1	r3c2	r3c3	r3c4	r3c5	r3c6	r3c7
r4c0	r4c1	r4c2	r4c3	r4c4	r4c5	r4c6	r4c7
r5c0	r5c1	r5c2	r5c3	r5c4	r5c5	r5c6	r5c7
r6c0	r6c1	r6c2	r6c3	r6c4	r6c5	r6c6	r6c7
r7c0	r7c1	r7c2	r7c3	r7c4	r7c5	r7c6	r7c7
r8c0	r8c1	r8c2	r8c3	r8c4	r8c5	r8c6	r8c7
r9c0	r9c1	r9c2	r9c3	r9c4	r9c5	r9c6	r9c7
r10c0	r10c1	r10c2	r10c3	r10c4	r10c5	r10c6	r10c7
r11c0	r11c1	r11c2	r11c3	r11c4	r11c5	r11c6	r11c7
r12c0	r12c1	r12c2	r12c3	r12c4	r12c5	r12c6	r12c7
r13c0	r13c1	r13c2	r13c3	r13c4	r13c5	r13c6	r13c7
r14c0	r14c1	r14c2	r14c3	r14c4	r14c5	r14c6	r14c7
r15c0	r15c1	r15c2	r15c3	r15c4	r15c5	r15c6	r15c7

- 8) PCM Output: This stage is responsible for reading the matrix at the specified (IAN) provided by the RGM sequencing block and transmitting it through the memory output ports-8 ports for a (16×8) architecture, 16

ports for a (32×8) architecture, and 32 ports for a (64×8) architecture. Each memory output port reads two contiguous rows, one element at a time. Consequently, it takes 16 clock cycles to read the entire matrix, regardless of the architecture. Each port's designated row is color-coded in Table II, clearly indicating the row allocation per port.

C. Matrix multiplier module

The matrix multiplier module performs large-scale matrix multiplications by multiplying a precoding matrix H (of sizes (16×8) , (32×8) , or (64×8) , depending on the configuration) with the user data vectors (X) from the ORAN. The precoding matrix (H) represents the characteristics of the channel, while the data vector (X), arranged as an (8×1) vector, enables spatial multiplexing across antenna layers.

The key components within the multiplier subsystem and their respective functions are as follows:

- 1) User data broadcaster: This module distributes resource elements (RE) from the ORAN U-plane as 32-bit coefficients. In an 8-layer configuration, these are arranged into an (8×1) vector (X) for multiplication with the channel matrix (H). The matrix (H) is divided into sub-matrices for easier handling. Each submatrix is divided into (2×8) blocks. This structure enables efficient broadcast of user data in 1:2 or 1:4 increments, ensuring seamless alignment with (H) during multiplication.
- 2) Dot product: The dot product module performs complex multiplications of the sub-matrices, such as a (2×8) channel matrix with an (8×1) user data vector, using an optimized Karatsuba approach [9]. Each element (h) in the channel matrix has a real part $a = Re(h)$ and an imaginary part $b = Im(h)$, while each data element (x) in the user matrix has a real part $c = Re(x)$ and an imaginary part $d = Im(x)$. The Karatsuba-based calculations (see Fig.4) proceed as follows:

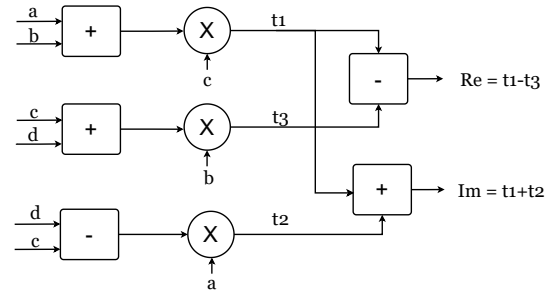


Fig. 4: Dot product of matrices

- a) Compute three intermediate values:

$$t_1 = c \times (a + b) \quad (1)$$

$$t_2 = a \times (d - c) \quad (2)$$

$$t_3 = b \times (c + d) \quad (3)$$

- b) Determine the real and imaginary outputs using equations Eq. 1, Eq. 2, and Eq. 3:

$$\text{Re} = t_1 - t_3 \quad (4)$$

$$\text{Im} = t_1 + t_2 \quad (5)$$

For example, the multiplication of (64×8) is split into four (16×8) multiplier modules. Each (16×8) unit computes eight dot products between (2×8) and (8×1) matrices, with each dot product resulting in a (2×1) matrix output.

- 3) Combiner/adder: This module aggregates the partial results generated from multiple dot products to form the final output as depicted in Fig.5.

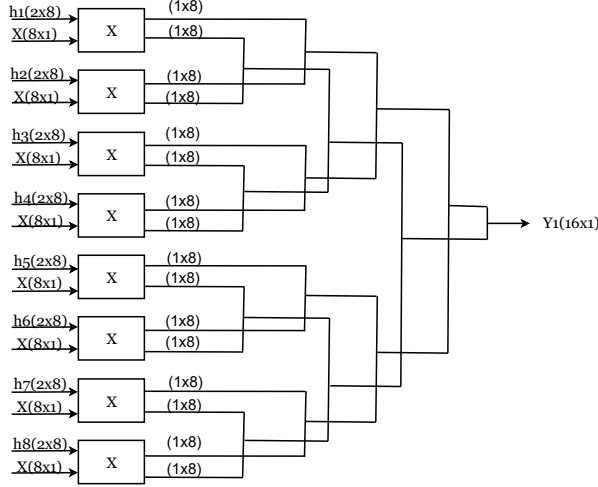


Fig. 5: Combiner/Adder

It takes the individual (2×1) outputs from each dot product in the matrix multiplier and combines them. The combined output will be transmitted as (Y) in sizes of (16×1) , (32×1) or (64×1) .

D. Precoder Tx to RX converter

The Tx and Rx precoders differ in the order of the matrix elements sent to the multiplier. While the Tx precoder transmits data in a specific sequence. In contrast, the Rx precoder memory uses a transposed version of the matrix, requiring a different data arrangement. This difference is clearly illustrated in the color-coded format shown in Table III.

TABLE III: RX precoder coefficient matrix output format

r0c0	r0c1	r0c2	r0c3	r0c4	r0c5	r0c6	r0c7	r0c8	r0c9	r0c10	r0c11	r0c12	r0c13	r0c14	r0c15
r1c0	r1c1	r1c2	r1c3	r1c4	r1c5	r1c6	r1c7	r1c8	r1c9	r1c10	r1c11	r1c12	r1c13	r1c14	r1c15
r2c0	r2c1	r2c2	r2c3	r2c4	r2c5	r2c6	r2c7	r2c8	r2c9	r2c10	r2c11	r2c12	r2c13	r2c14	r2c15
r3c0	r3c1	r3c2	r3c3	r3c4	r3c5	r3c6	r3c7	r3c8	r3c9	r3c10	r3c11	r3c12	r3c13	r3c14	r3c15
r4c0	r4c1	r4c2	r4c3	r4c4	r4c5	r4c6	r4c7	r4c8	r4c9	r4c10	r4c11	r4c12	r4c13	r4c14	r4c15
r5c0	r5c1	r5c2	r5c3	r5c4	r5c5	r5c6	r5c7	r5c8	r5c9	r5c10	r5c11	r5c12	r5c13	r5c14	r5c15
r6c0	r6c1	r6c2	r6c3	r6c4	r6c5	r6c6	r6c7	r6c8	r6c9	r6c10	r6c11	r6c12	r6c13	r6c14	r6c15
r7c0	r7c1	r7c2	r7c3	r7c4	r7c5	r7c6	r7c7	r7c8	r7c9	r7c10	r7c11	r7c12	r7c13	r7c14	r7c15

This reordering is necessary due to the (2×8) dot product units in the multiplier module, which can only process 8

columns of dot products at a time. The converter module arranges the transposed matrix to meet this processing constraint, allowing the main module of the Tx precoder to be easily used for Rx operations. The state diagram shown in Fig.6 describes the read and write finite state machine (FSM) of the Tx to RX converter module.

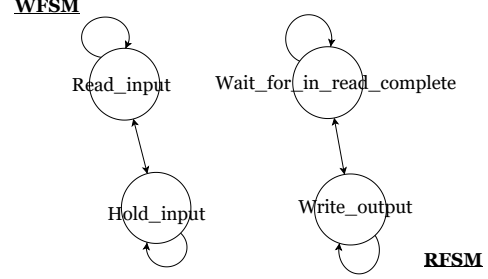


Fig. 6: Read and Write FSM state diagram

The function of the write FSM is as follows:

- 1) Read_input: Load the incoming beamforming matrix in the TX sequence.
- 2) Hold_output: Once the input read is completed, hold this matrix until the output side can make a copy of it.

The function of the read FSM is as follows:

- 1) wait_for_in_read_complete: Wait until the input read is completed and then make a copy of the read matrix.
- 2) write_output: write the copy in the RX output sequence format.

III. DATA FLOW

A. Algorithmic description of the TX precoder module

The data flow in the TX precoder module is enumerated as follows (See Fig.7):

- 1) Read a control packet from oran_config_in and find out if the beam id has appeared before or is this the first time this slot.
- 2) If the beam id is new, allocate a new IAN for it, or if the beam is old, forward the allocated IAN to the read data pipeline.
- 3) Read the beam coefficients for one layer using the data in port. Retrieve the IAN forwarded by the control pipeline. Store the data at the designated matrix address in the PCM BRAM buffer, following the order required for the multiplier.
- 4) Meanwhile, the subsequent stages of the control pipeline store the scheduling information in the RGM BRAM buffer.
- 5) Continue until a new control packet indicates a slot change. If both buffers are full, wait for one to free up; otherwise, alternate between writing and reading buffers.
- 6) Upon receiving a read_trigger, check the availability of the pipeline. If busy, acknowledge with a valid and ready signal and complete two reads before the next response.

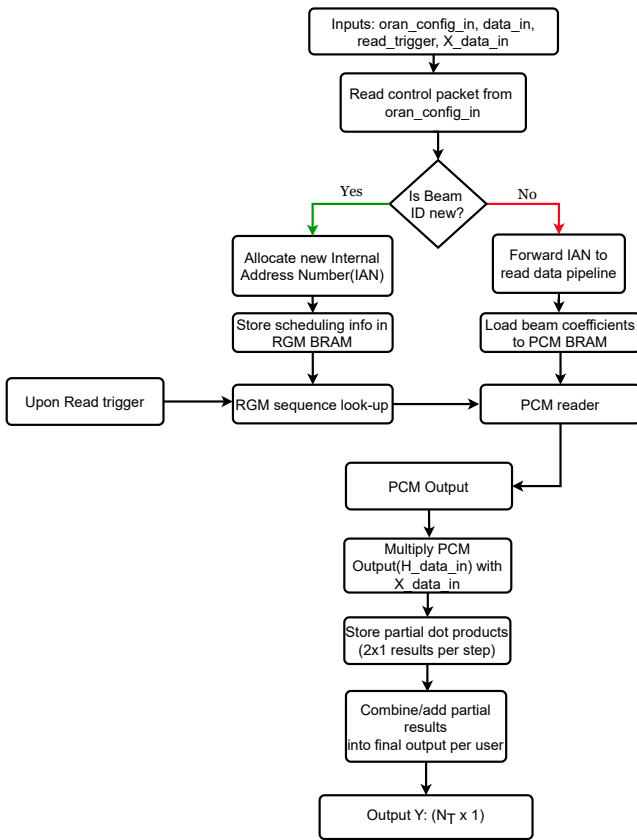


Fig. 7: Algorithmic description of the TX precoder

- 7) When it is triggered, read the RGM to determine the sequence of matrices for the multiplier.
- 8) Communicate the sequence and matrix usage count to the multiplier via mult_cfg port and start reading the matrix from the PCM.
- 9) The PCM data is then multiplied with X_data_in to perform the necessary beamforming operations.
- 10) Partial dot products ((2 × 1) results per step) are temporarily stored as intermediate results.
- 11) The stored partial results are combined or added to generate the final output for each user.
- 12) The final output, represented as (Y), is produced as a vector with dimensions (16 × 1), (32 × 1) or (64 × 1), depending on the configuration of the system.

IV. TESTING AND EVALUATION

A. Simulation level

The precoder memory and multiplier modules were first tested individually using MATLAB-generated reference data and RTL simulations on the Xilinx Vivado platform. The functionality of each module was checked by comparing its output with the MATLAB results, to ensure that the modules performed as expected. To have an efficient data transfer towards and from the module, we adopt an AXIS handshake protocol for the I/O data ports. Inputs were applied directly

to each module, and outputs were verified individually. After successful standalone testing, the modules were integrated into end-to-end transmitter and receiver chains to observe system-level performance.

B. Hardware Testing

After successful simulations, the precoder modules were integrated into the transmitter and receiver chain for hardware testing. Both wired and wireless configurations were tested using vector signal analyzer (VSA) and observed the system's performance and signal quality across different setups. Multiple stress tests were also performed to assess the robustness of the system, which shows that it can handle up to precoding of 48 users within 500μs.

V. RESULTS

Theoretical analysis based on the parameters shown in Table IV shows that the read-out time of the memory module in the best case scenario is approximately 430μs, which fits within the 500μs slot boundary. This timing allows the precoder to operate at resource element-level granularity. The calculations below verify this performance.

TABLE IV: Latency and Timing parameters

Parameter	Value
Slot Boundary Time (S_T)	500μs
Total No. of PRBs (T_{PRB})	273
1 RB	12 RE
Total no. users (T_u)	64
Latency to Load One Matrix (T_{load})	16 clk cycles
Latency to Multiply One Matrix (T_{mult})	2 clk cycle
Time Period of Multiplier (T_{clk})	4 ns
Max no. of H matrices (n_H)	64
Max no. of user matrices (n_X)	$273 \times 14 \times 12 = 45864$
Total number of multiplications (N_{mult})	$\max(n(H), n(X)) = 45864$

Considering there are 64 matrices across all 14 symbols, the optimal latency achievable is calculated using Eq.6 and Eq.7. For each matrix denoted by n_i , ($i = 1, 2, \dots, 64$), the PRBs follow the inequality given by Eq.6.

$$(n_1 + n_2 + \dots + n_{64}) \leq T_{PRB} \quad (6)$$

The matrix corresponding to the any user n_k is calculated using the formula given by Eq.7.

$$\left(\frac{1}{T_{clk}} + T_{mult} \times 1 \text{ RB} \right) \times \sum_{i=1}^k n_i + (T_{load} \times T_{PRB}) \text{ clk cycles} \quad (7)$$

Using Eq.6 and Eq.7 the upper bound per symbol is determined to be 7644.25 clk cycles, which corresponds to 107030 clk cycles per slot, for a total of 14 symbols. Therefore, the

TABLE V: Timing analysis for different system configurations

	Setup Time (ns)	Hold Time (ns)	Pulse Width (ns)
16x8 system	1.133	0.026	1.105
32x8 system	1.219	0.027	1.105
64x8 system	1.831	0.045	1.105

TABLE VI: Hardware resource utilization for different system configurations

Resource	16x8 System			32x8 System			64x8 System		
	Utilization	Available	Utilization %	Utilization	Available	Utilization %	Utilization	Available	Utilization %
LUT	2412	522720	0.46%	3477	522720	0.67%	5635	522720	1.08%
LUTRAM	48	161280	0.03%	48	161280	0.03%	48	161280	0.03%
FF	2739	1045440	0.26%	3928	1045440	0.38%	6145	1045440	0.59%
BRAM	22.50	984	2.284%	38.50	984	3.91%	70.50	984	7.16%
DSP	192	1968	9.75%	384	1968	19.5%	768	1968	39.00%

time required per slot for the multiplier operation is calculated as $430\mu s$, which is within the $500\mu s$ slot duration.

The analysis demonstrates that the maximum multiplier count, N_{mult} , occurs under a worst-case scenario where users are allocated alternately on the resource grid. In such a case, every alternating resource element is assigned to a new user, requiring a new matrix multiplication and hence loading of a new matrix in to the memory. However, if the user allocation pattern is different, the multiplier count can be lower, which may reduce the overall latency.

The timing analysis for the (16×8) , (32×8) , and (64×8) configurations, presented in Table V, demonstrates that the setup time, hold time, and pulse width for each system meet the necessary timing constraints. Specifically, synchronization and latency checks confirm reliable operation with the multiplier operating at 250 MHz and memory access at 312.5 MHz. This ensures that the system works efficiently within the required timing limits.

Table VI provides an overview of the resource utilization across key hardware components (LUTs, FFs, BRAMs, and DSP blocks) for the (16×8) , (32×8) , and (64×8) configurations. For the (16×8) system, the utilization of DSPs, LUTs, FFs, and BRAMs is 9.75%, 0.46%, 0.26%, and 2.28%, respectively. This suggests that the (16×8) configuration utilizes resources efficiently with relatively low consumption, indicating a well-balanced design. In the (32×8) configuration, DSP utilization increases to 19.5%, and LUTs, FFs, and BRAMs consume 0.67%, 0.38%, and 3.91%, respectively. The higher DSP utilization in this configuration is expected due to the increase in processing demand. Finally, the (64×8) system shows a significant increase in DSP usage, reaching 39%, while LUTs, FFs, and BRAMs account for 1.08%, 0.59%, and 7.16%, respectively. Despite the increase in resource consumption, particularly in DSPs and BRAMs, the system still operates within the capacity of the hardware platform xczu19eg-ffvd-1760-3-e (Zynq ultrascale + MPSoC family), confirming that the design scales efficiently while adhering to resource constraints. This analysis demonstrates that the system remains optimized for performance in varying configurations, operating efficiently without exceeding hardware limits. With 4 active layers, the throughput achieved for both (16×8) and (32×8) channel configurations is $1.2Gbps$, confirming the system's effective use of available resources.

VI. CONCLUSION

This paper presented an optimized precoder design for 5G NR, demonstrating efficient use of FPGA resources. With a throughput of $1.2Gbps$ in both (16×8) and (32×8) configurations, the system achieves optimal performance using only four active layers. The design meets strict latency and resource constraints, confirming its feasibility for real-time 5G deployment. The flexibility across different configurations highlights the precoder's robustness for future 5G and beyond applications.

ACKNOWLEDGMENT

The authors extend their gratitude to the Department of Telecommunications (DOT), India for funding the 5G Testbed project.

REFERENCES

- [1] S. Parkvall, E. Dahlman, A. Furuskar, and M. Frenne, "NR: The new 5G radio access technology," *IEEE Communications Standards Magazine*, vol. 1, no. 4, pp. 24–30, 2017.
- [2] J. K. S, K. B. S. D. S. Praneeth, K. B. S. M. D. S. S. Prasanth, R. Singh, S. R. Santhosh Kumar, R. Surya, S. P. C. D'silva, P. Bharath, H. Prakash, L. S, R. Devara, Parthiban, A. Gundlapalle, S. Singh, A. P. P. V, K. Bhukya, N. Jayapal, J. Saini, S. Yogesh, A. KR, D. Naveen, R. K. Ganti, and R. Budhiraja, "Physical layer design of a 5G NR base station," in *2024 National Conference on Communications (NCC)*, 2024, pp. 1–6.
- [3] M. Hemnani, S. Palekar, P. Dixit, and P. Joshi, "Hardware optimization of complex multiplication scheme for DSP application," in *2015 International Conference on Computer, Communication and Control (IC4)*, 2015, pp. 1–4.
- [4] A. Haqiqatnejad, J. Krivochiza, J. C. M. Duncan, S. Chatzinotas, and B. Ottersten, "Design optimization for low-complexity FPGA implementation of symbol-level multiuser precoding," *IEEE Access*, vol. 9, pp. 30 698–30 711, 2021.
- [5] M. K. Jaiswal and N. Chandrachoodan, "FPGA-based high-performance and scalable block LU decomposition architecture," *IEEE Transactions on Computers*, vol. 61, no. 1, pp. 60–72, 2012.
- [6] "IIT Madras 5G Testbed," <http://www.5gtbitm.in/>, Accessed: 2023-09-11.
- [7] WG-4, "O-RAN Working Group 4 (Open Fronthaul Interfaces WG) Control, User and Synchronization Plane Specification," Open RAN Alliance, Technical Specification (TS), 2022, o-RAN.WG4.CUS.0-v11.00.
- [8] 3GPP, "Physical Channels and Modulation," 3rd Generation Partnership Project (3GPP), Technical Specification (TS) 38.211, 2018, version 15.3.0.
- [9] P. Paz and M. Garrido, "Efficient implementation of complex multipliers on FPGAs using dsp slices," *Journal of Signal Processing Systems*, vol. 95, no. 4, pp. 543–550, 2023.